The Astrophysical Journal Letters, 888:L16 (7pp), 2020 January 10 https://doi.org/10.3847/2041-8213/ab61fe

Relationship between Current Filaments and Turbulence During a Turbulent Reconnection

Z. Z. Chen[1,2], T. Y. Wang[3], Y. Yu[1,2], and F. Chen[1,2]
[1] School of Space and Environment, Beihang University, Beijing, People's Republic of China; zuzhengchen@gmail.com
[2] Key Laboratory of Space Environment Monitoring and Information Processing, Ministry of Industry and Information Technology, Beijing, People's Republic of China
[3] RAL Space, STFC, Oxfordshire, UK
Received 2019 October 20; revised 2019 December 6; accepted 2019 December 11; published 2020 January 9

Abstract

Both magnetic reconnection and turbulence can play crucial roles in space plasmas. The current layers, developing during magnetic reconnection, can collapse into various small-scale coherent structures, such as current filaments. These current filaments can significantly modulate the kinetic-scale turbulence. However, the quantitative correlation between the current filaments and turbulence remains unknown so far. In this study, we statistically analyze such a relation during a turbulent reconnection in the magnetotail. We find that the kinetic-scale turbulence has a good correlation with the current-density variation $\left(J' = \left|\frac{dJ}{dt}\right|\right)$. Specifically, (1) the slope of the kinetic-scale power spectral density (PSD), denoted as $S_{\rm PSD}$, decreases with J', exhibiting an empirical relation $S_{\rm PSD} = -0.54\ln(J') - 1.36$; (2) the correlation between turbulence intensity (PSD) and J' is best at the frequency range 0.02–0.32 ω_{ce} (electron cyclotron frequency); (3) the turbulence intensity (PSD) increases with J', exhibiting an empirical relation PSD $= J'^{k} \bullet e^{b}$; and (4) the k of these fitting functions roughly decreases with frequency. These results can advance our understanding of the interplay between magnetic reconnection and turbulence.

Unified Astronomy Thesaurus concepts: Interplanetary turbulence (830); Space plasmas (1544); Plasma jets (1263)

1. Introduction

Magnetic reconnection, one of the most fundamental plasma processes in solar-terrestrial space, is frequently observed in the heliospheric current sheet (He et al. 2009), solar wind (Gosling et al. 2005), magnetosheath (Retinò et al. 2007; Vörös et al. 2017), magnetopause (Burch et al. 2016b; Fuselier et al. 2017; Peng et al. 2017; Webster et al. 2018; Fu et al. 2019b), and magnetotail (Torbert et al. 2018). It happens in the diffusion region, where the electron diffusion region (EDR) is embedded inside the ion diffusion region (IDR) due to the different ion and electron motions (Øieroset et al. 2001; Eastwood et al. 2010; Burch et al. 2016b; Chen et al. 2016; Cao et al. 2017; Fu et al. 2017). Magnetic reconnection not only changes magnetic topology (Pontin & Craig 2006; Pontin 2011; Chen et al. 2019c; Fu et al. 2019a), but also effectively converts magnetic energy to kinetic and thermal energy of plasmas (Yamada et al. 2010; Fu et al. 2011, 2012a, 2013b, 2019b, 2019c; Li et al. 2015; Chen et al. 2019a). Thus, magnetic reconnection is responsible for many explosive energy release phenomena in space, such as magnetospheric substorms and coronal mass ejections (Chen & Shibata 2000; Angelopoulos et al. 2008; Fu et al. 2012b, 2013a; Liu et al. 2018b; Xu et al. 2018b).

Plasma turbulence is another fundamental phenomenon of space plasma, which plays a crucial role in distributing the fluctuation energy across scales (Tu & Marsch 1995; Borovsky et al. 1997; Sahraoui et al. 2009; Alexandrova et al. 2013; Huang et al. 2014; Chen 2016; Olshevsky et al. 2018; He et al. 2019). Through the cascade process, the energy injected at large scales can be transferred down to kinetic scales and then dissipate. Magnetic reconnection can drive plasma turbulence (Eastwood et al. 2009; Karimabadi et al. 2013; Wang et al. 2016; Fu et al. 2017; Ergun et al. 2018; Liu et al. 2019b). Simulation and observation efforts have been made to study turbulence in magnetic reconnection. Kinetic simulations demonstrate that the current layer, formed during reconnection, becomes intense and then breaks into various small-scale coherent structures, such as flux ropes and current filaments (Che et al. 2011; Daughton et al. 2011; Liu et al. 2013; Chen et al. 2019d; Lu et al. 2019; Zhu et al. 2020). These coherent structures, along with electromagnetic turbulence, can increase the reconnection rate (Che et al. 2011; Daughton et al. 2014), accelerate electrons (Li et al. 2014; Guo & Giacalone 2015; Olshevsky et al. 2018; Xu et al. 2018a; Liu & Fu 2019; Liu et al. 2019c; Lu et al. 2019; Zhu et al. 2019), and dissipate energy (Karimabadi et al. 2013; Olshevsky et al. 2015; Wan et al. 2015; Yang et al. 2017; Chen et al. 2019b; Huang et al. 2019). Moreover, the developed turbulence associated with these current filaments can drive smaller-scale reconnection (Retinò et al. 2007; Olshevsky et al. 2013; Chen et al. 2019c), which can make the magnetic spectrum steepen at the scale of the reconnecting current sheets (Stawarz et al. 2019). In the magnetosheath turbulence, Stawarz et al. (2019) examined the statistics of current structures using data from the *Magnetospheric Multiscale* (*MMS*) mission (Burch et al. 2016a) and found that the prevalence of electron-scale current sheets is favorable for electron reconnection. The complex web of current filaments has been also observed in the IDR by the *Cluster* mission (Eastwood et al. 2009; Fu et al. 2017). In those observations, the power-spectrum density of the kinetic-scale turbulence is strong when the current density is large, while the power-spectrum density of the kinetic-scale turbulence is weak when the current density is small (see Figure 2(c) in Fu et al. 2017). These studies (Che et al. 2011; Fu et al. 2017) suggest that the currents can significantly modulate the kinetic-scale turbulence. However, the quantitative relation between currents and turbulence, namely the relational expression between currents and turbulence characteristics, has not been studied so far.

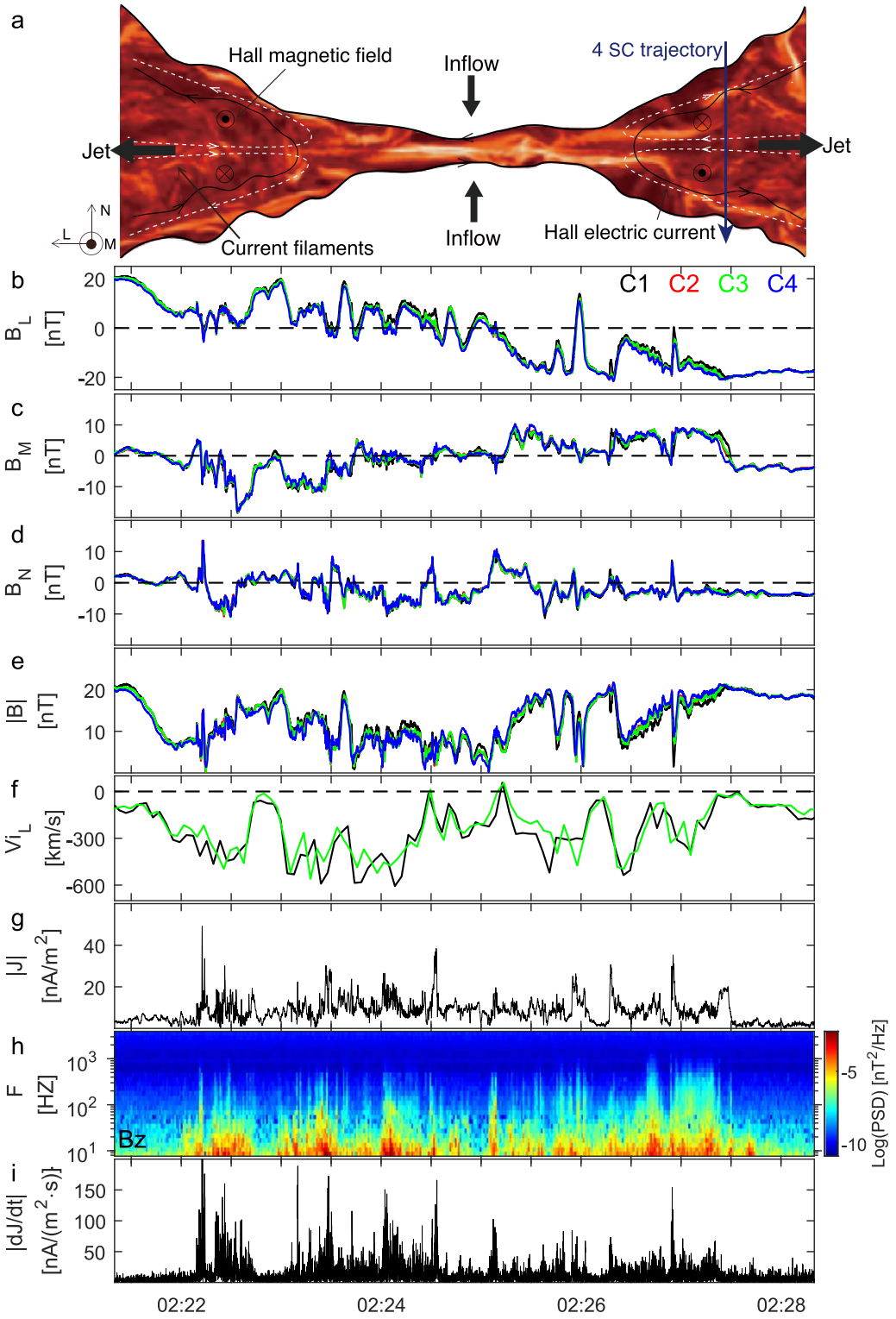

Figure 1. Ion diffusion region encountered by *Cluster* in the terrestrial magnetotail. Data are shown in local current sheet coordinates (LMN). With respect to geocentric solar magnetospheric (GSM) coordinates, $L = (0.895, -0.441, 0.068)$, $M = (0.445, 0.892, -0.072)$, and $N = (-0.029, 0.094, 0.994)$. (a) Schematic of the ion diffusion region. (b)–(e) Magnetic field (b) B_L component, (c) B_M component, (d) B_N component, and (e) magnitude ($|\boldsymbol{B}|$). (f) V_L component of reconnection jet velocity. In (b)–(f), the measurements are from *Cluster 1–4*, presented in black, red, green, and blue, respectively. For *Cluster 2* and *4*, the velocity measurements are unavailable. (g) The current density derived from curlometer method. (h) Turbulence power spectrum of B_Z measured by *Cluster 4*. (i) The current-density variation (absolute value of total derivative of current density, $J' = \left|\frac{dJ}{dt}\right|$) calculated from $\left|\frac{J(t)-J(t-\Delta t)}{\Delta t}\right|$, where Δt is the sample interval of current density.

Investigating such a quantitative relation can advance our understanding of magnetic reconnection and turbulence. In this study, we statistically investigate how the current filaments affect the kinetic-scale turbulence inside the IDR.

2. Event Overview

In this study, data are from the *Cluster* mission (Escoubet et al. 2001). Particularly, the magnetic field data are from the

Fluxgate Magnetometer experiment; the plasma data are from the Cluster Ion Spectrometry experiment; and the wave data are from the Spatial and Temporal Analysis of Field Fluctuations (STAFF).

A reconnection event in the Earth's magnetotail was observed by *Cluster* on 2003 October 9, at about 02:25 UT, when the four *Cluster* spacecraft, forming a regular tetrahedron with size of ~200 km, were located at (−15.6, 9.2, 3.1) Re (Earth radii) in GSM coordinates. This event has been identified as an IDR encounter and analyzed on the general properties of turbulence by Eastwood et al. (2009). Then, Fu et al. (2017) analyzed the intermittent energy dissipation in this event and illustrated that the current can significantly modulate the kinetic-scale turbulence.

Figure 1 is an overview of this event. Magnetic field and ion velocity are shown in the local boundary normal (LMN) coordinates, given by Eastwood et al. (2009), where L points earthward, N is normal to the current sheet, and M completes the right-handed coordinate system. The four spacecraft crossed the IDR from north to south (see the blue line in Figure 1(a)), reflected by the positive to negative reversal in B_L (Figure 1(b)). The magnetic field fluctuations in B_L (Figures 1(b)) follow a $-5/3$ power law in the inertial range (Eastwood et al. 2009), suggesting the existence of turbulence in the IDR (Lazarian & Vishniac 1999; Daughton et al. 2011; Karimabadi et al. 2013; Guo et al. 2015). The similar magnetic fields (Figures 1(b)–(e)) measured by four spacecraft suggest that the inter-spacecraft separations are small, and thus the linear assumption of magnetic fields (Dunlop et al. 2002; Fu et al. 2015) around the spacecraft tetrahedron is reliable. During the IDR crossing, the Hall magnetic field without a guide field (see the bipolar variation in B_M in Figure 1(c)) and the tailward ion flow (Figure 1(f)) were detected. In addition, the magnitude of magnetic fields sometimes approaches 0 nT (Figure 1(e)), suggesting that magnetic nulls exist in this event. Fu et al. (2017) applied the First-Order Taylor Expansion (FOTE) method (Fu et al. 2015, 2016) to search for magnetic nulls, and found that these magnetic nulls are mainly spiral nulls (see Figure 3 in Fu et al. 2017 for more details).

We apply the FOTE method (Fu et al. 2015, 2016) to reconstruct the magnetic topology of one of these spiral nulls, i.e., at 02:26:55.50 UT, as done in previous studies (Fu et al. 2016, 2017, 2019a; Chen et al. 2018). To better reveal the topological features of these nulls, the eigenvector coordinates (e_1, e_2, e_3) obtained from the Jacobian matrix ∇B are used (Fu et al. 2015, 2019a; Liu et al. 2018a, 2019a, 2019d; Chen et al. 2019c, 2019b, 2019d; Wang et al. 2019), where e_1 is the real eigenvector, e_3 is obtained from $e_3 = e_1 \times Z_{\rm GSM}$, and e_2 completes the right-hand coordinate system $e_2 = e_3 \times e_1$. In (e_1, e_2, e_3) coordinates, we trace a few points around the spiral null to obtain the topology in Figure 2. The color scale in Figure 2 denotes the magnetic field strength $|B|$ and the blue arrows denote the magnetic field direction. The reconstructed magnetic topology is consistent with theoretical models (Parnell et al. 1996; Fu et al. 2015). Figure 2(a) presents the 3D magnetic topology, which clearly shows the "spiral" features of the null. Looking along the direction ($-e_1$, 0, 0), we find that the spiral null becomes a magnetic island or flux rope (Figure 2(b)), namely, an "O-line" topology (Fu et al. 2016; Wang et al. 2017; Chen et al. 2019b).

We calculate the current density using the curlometer technique (Dunlop et al. 2002). As can be seen, a series of

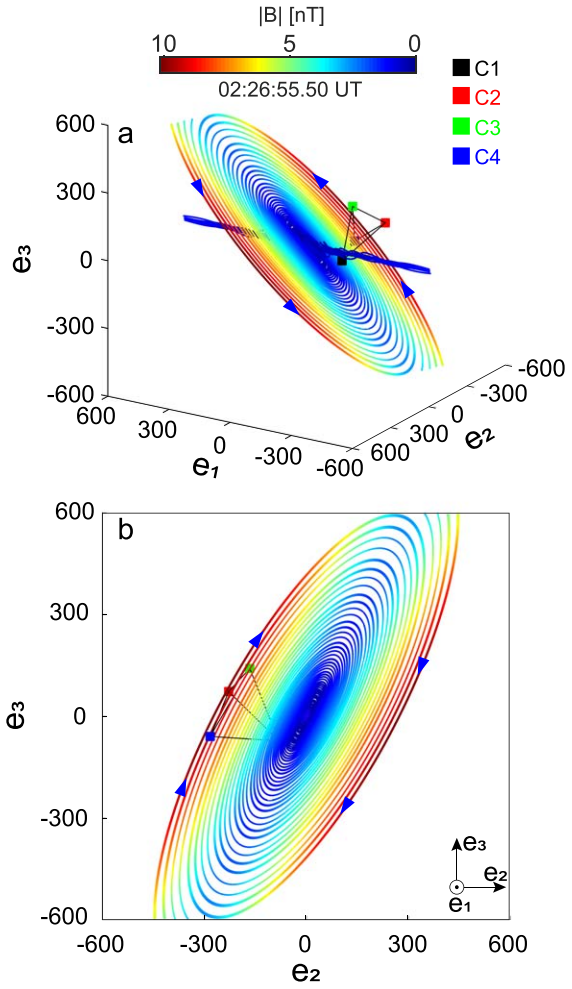

Figure 2. Reconstructed magnetic topology of one of these spiral nulls using the FOTE method, i.e., at 02:26:55.50 UT. (a) The 3D magnetic topology of the spiral null. (b) The 2D view of the topology along the direction ($-e_1$, 0, 0). The blue arrows denote the magnetic field directions, and the color scale denotes the magnetic field strength. The color rectangles represent C1 (black), C2 (red), C3 (green), and C4 (blue), respectively.

current filaments (Figure 1(g)) with scales of ~10–20 d_e (electron inertial length $d_e = c/\omega_{\rm pe} \approx 25$ km; see the Supporting Information of Fu et al. 2017 for details) was detected in the IDR. The power-spectrum densities of turbulence in these current filaments are larger than that averaged during the reconnection current sheet (Figures 1(g)–(h), see Figure 2(e) in Fu et al. 2017 for details), indicating that the current affects the kinetic-scale turbulence (Che et al. 2011; Fu et al. 2017). However, turbulence power-spectrum densities in stronger current filaments are not always more intense than those in weaker current filaments (Figures 1(g)–(h)), which suggests that current density may not be the only factor determining the kinetic-scale turbulence. Simulations demonstrated that electron shear-driven instability, feeding on electron flow-velocity gradients, can result in the kinetic-scale turbulence in magnetic reconnection (Che et al. 2011; Jain et al. 2017). In the IDR, the current is primarily driven by electrons, suggesting that electron flow-velocity gradients are approximately equated with current-density gradients. In addition, current-density gradients can make current layers evolve into a strong turbulent state (Coppi 1965; Drake et al. 1994). Thus, we examine whether the kinetic-scale turbulence correlates with the current-

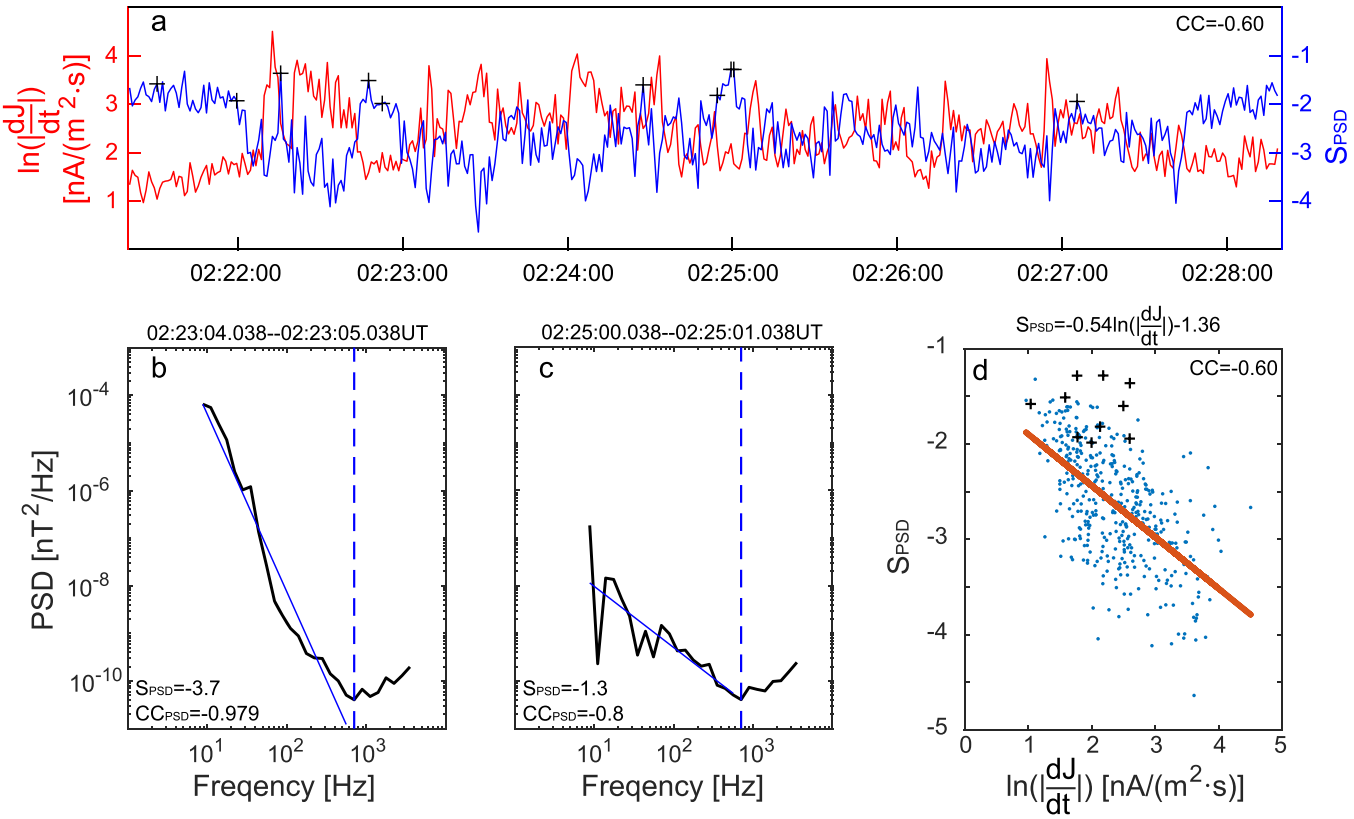

Figure 3. Relation between the current-density variation $\left(\left|\frac{dJ}{dt}\right|\right)$ and the slope ($S_{\rm PSD}$) of turbulence power-spectrum density (PSD) of B_z. (a) The Napierian logarithm of $\left|\frac{dJ}{dt}\right|$ $\left(\ln\left(\left|\frac{dJ}{dt}\right|\right)\right.$; red) and the slope of turbulence PSD ($S_{\rm PSD}$; blue). $\left|\frac{dJ}{dt}\right|$ are averaged during each sampling interval of $S_{\rm PSD}$. (b) and (c) Examples of fitting of PSD with (b) high-correlation coefficients ($\rm CC_{PSD} = -0.85$) and (c) low-correlation coefficients ($\rm CC_{PSD} > -0.85$). (d) Scatter diagram of $\ln\left(\left|\frac{dJ}{dt}\right|\right)$ and $S_{\rm PSD}$, with fitting function (red oblique line). The black crosses in panels (a) and (d) denote these points with $\rm CC_{PSD} > -0.85$.

density variations, which is expressed as the absolute value of total derivative of current density $J' = |\frac{dJ}{dt}|$ in this paper.

Figure 1(i) shows the current-density variation (J'), calculated from $\left|\frac{J(t)-J(t-\Delta t)}{\Delta t}\right|$, where Δt is the sample interval of current density. We find that the turbulence power density and current-density variation (J') are well correlated, where the turbulence power density increases with the increase of J' (Figures 1(h)–(i)). In the next section, we perform statistical analyses during the IDR crossing to study the quantitative relation between current-density variation (J') and turbulence properties, including power-spectrum density (PSD) and its scaling.

3. Statistical Results

Figure 3 shows the relations between the current-density variation (J') and the slope of the PSD for the z-component of the magnetic field. The slope, hereinafter referred to as $S_{\rm PSD}$, is obtained by the least-squares fitting of the PSD data (Figures 3(b)–(c)) from STAFF measurements with a 1 s resolution. Since the data are unreliable at very-high frequencies (higher than the frequency marked by the vertical blue dashed lines in Figures 3(b)–(c)), we obtain the slope by fitting the PSD data below the frequency marked by the vertical blue dashed line (the frequency marked by blue dashed line is not included). The $\rm CC_{PSD}$ shown in the lower left corner of Figures 3(b)–(c) is the correlation coefficients. Figure 3(c) shows that measurements may also be unreliable at frequencies less than the frequency marked by the vertical blue dashed line (e.g., sharp dip at ∼10 Hz), leading to $\rm CC_{PSD} > -0.85$. There are 10 points with $\rm CC_{PSD} > -0.85$ (marked by black crosses in Figure 3(a)), much less than the total number of measurement points (419 points) during the IDR crossing. Also, we note that the sampling rate of J' is higher than that of $S_{\rm PSD}$, thus we average J' over each sampling interval of $S_{\rm PSD}$. As can be seen, the Napierian logarithm of $|\frac{dJ}{dt}|$ $(\ln\left(\left|\frac{dJ}{dt}\right|\right)$; red curves) and the $S_{\rm PSD}$ (blue curves) are clearly anti-correlated with a correlation coefficient of −0.60 (Figure 3(a)). Then we discard the points with $\rm CC_{PSD} > -0.85$, marked by black crosses in Figure 3(d). Figure 3(d) shows the $S_{\rm PSD}$ plotted as a function of $\ln(J')$. We perform a linear least-squares fitting to obtain their relation $S_{\rm PSD} = -0.54\ln(J') - 1.36$. As can be seen, the correlation coefficient is still −0.60, suggesting that discarding these 10 points with $\rm CC_{PSD} > -0.85$ almost does not affect the fitting results. The $S_{\rm PSD}$ decreases linearly with the logarithm of J', suggesting that large J' steepens the spectral index and affects the dissipation scale.

In order to study how the current-density variation (J') affects the turbulence intensity, we perform cross-covariance analyses between the Napierian logarithm of turbulence PSD ($\ln(\rm PSD)$) at each frequency channel and Napierian logarithm of J' ($\ln(J')$). The results of the cross-covariance analyses (Figure 4(a)) show that the correlation is prominent (correlation coefficient $(r) \geqslant 0.45$) at low frequency ($f < 120$ Hz), and occurs when the $\ln(\rm PSD)$ at each frequency lags behind $\ln(J')$ by 0 s. This suggests that the correlation between turbulence PSD and J' is best at the frequency range 0.02–0.32 ω_{ce}

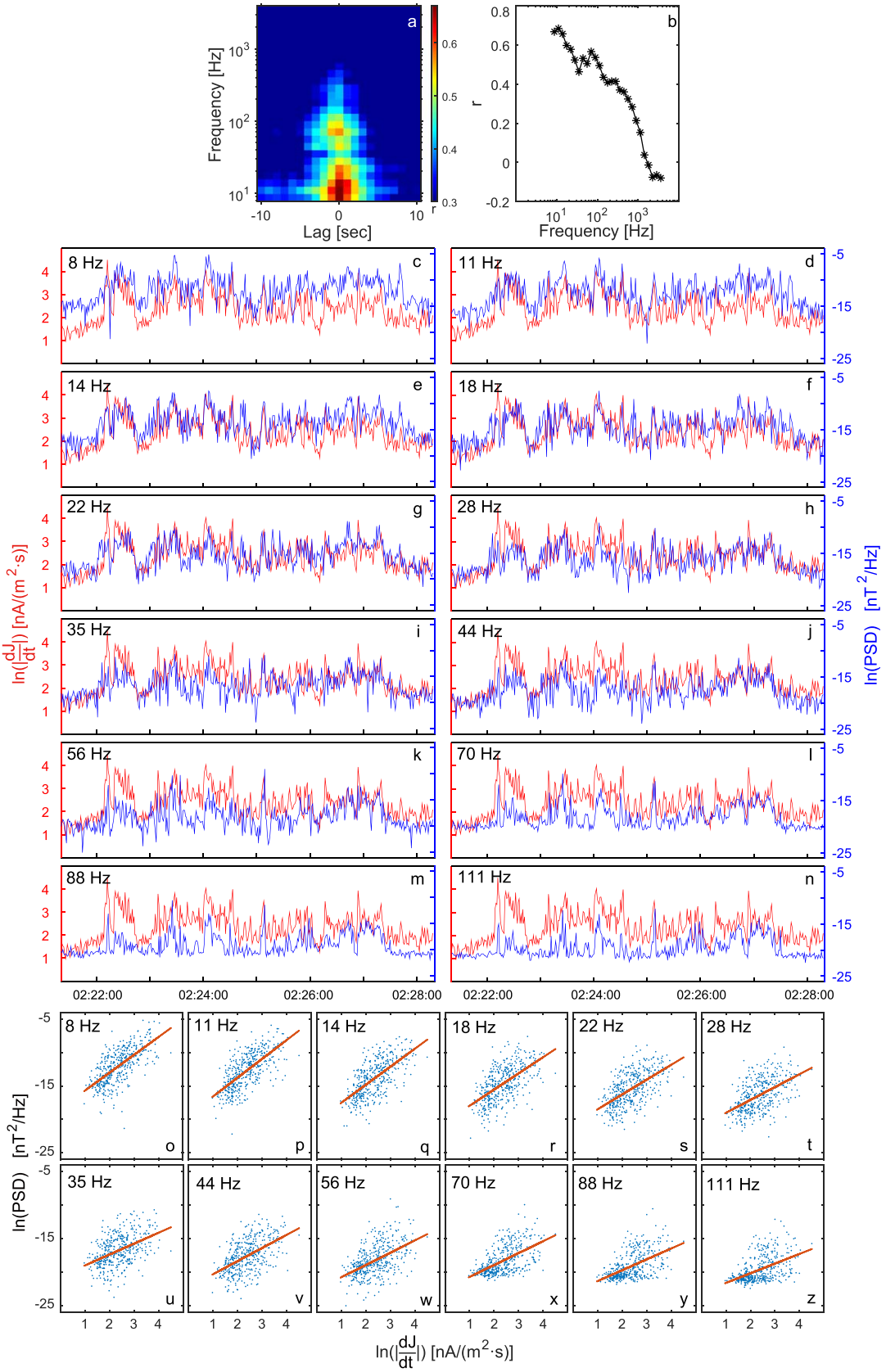

Figure 4. Cross-covariance analysis between the Napierian logarithm of PSD (ln (PSD)) at each frequency and Napierian logarithm of $\left|\frac{dJ}{dt}\right|\left(\ln\left(\left|\frac{dJ}{dt}\right|\right)\right)$. (a) Cross-covariance correlation coefficients between ln (PSD) at each frequency and $\ln\left(\left|\frac{dJ}{dt}\right|\right)$. (b) Cross-covariance correlation coefficients at lag = 0. (c)–(n) The Napierian logarithm of $\left|\frac{dJ}{dt}\right|$ $\left(\ln\left(\left|\frac{dJ}{dt}\right|\right)\right)$; red) and the Napierian logarithm of turbulence PSD (ln (PSD); blue) between 8 and 111 Hz. (o)–(z) Scatter diagram of $\ln\left(\left|\frac{dJ}{dt}\right|\right)$ and ln (PSD) between 8 and 111 Hz, with fitting functions (red oblique line).

Table 1
Correlation Coefficient (r), Slope (k), and Intercept (b) of Fitting Functions between 8 and 111 Hz

f (Hz)	8	11	14	18	22	28	35	44	56	70	88	111
r	0.67	0.68	0.66	0.60	0.58	0.52	0.46	0.53	0.50	0.57	0.54	0.49
k	2.67	2.81	2.69	2.42	2.21	1.92	1.63	1.96	1.84	1.78	1.62	1.45
b	−18.35	−19.36	−20.20	−20.39	−20.69	−20.94	−20.63	−22.28	−22.60	−22.52	−22.97	−23.07

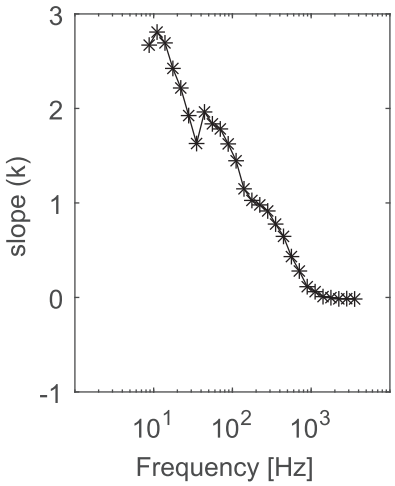

Figure 5. Slope (k) of the fitting function between ln (PSD) at each frequency and $\ln\left(\left|\frac{dJ}{dt}\right|\right)$ as a function of frequency.

(electron cyclotron frequency $\omega_{ce} \sim 370$ Hz). Except at ∼35 and ∼111 Hz, the correlation coefficients (r) are all larger than 0.5. Moreover, the correlation coefficient at lag = 0 roughly decreases with the increase of frequency (Figure 4(b)). As can be seen, ln (PSD) (blue curves) scales proportionally with ln (J') (red curves) at these 12 frequency channels (Figures 4(c)–(n)). Then we carried out a linear least-squares fitting of ln (PSD) at these 12 frequency channels and ln (J') to $\ln(\text{PSD}) = k \ln(J') + b$ (Figures 4(o)–(z)), where k and b are the slope and intercept of these fitting functions, respectively. The correlation coefficient (r), slope (k) and intercept (b) at these 12 frequency channels are shown in Table 1. Therefore, the PSD increases with J', following the power function $\text{PSD} = J'^k \cdot e^b$. As can be seen, the slope (k) of these fitting functions roughly decreases with frequency (Figure 5), and the intensity of lower-frequency fluctuation varies more dramatically with J'. The good correlation between J' and the PSD at low frequency suggests the existence of large-scale structures, while the good correlation between J' and the PSD at high frequency suggests the existence of small-scale turbulent fluctuations. Therefore, the slope (k) for low frequencies is higher than the slope for high frequencies, suggesting that the large-scale fluctuations should have significantly larger amplitudes compared to the much smaller-scale fluctuations.

4. Summary and Discussion

We perform statistical analyses to investigate the relationship between current filaments and turbulence during a turbulent reconnection event in the magnetotail, and find that turbulence is associated with the current-density variation (J'). Specifically, (1) the slope of kinetic-scale turbulence PSD decreases with increasing J', following the logarithmic function $S_{\text{PSD}} = -0.54 \ln(J') - 1.36$; (2) the correlation between turbulence power density (PSD) and J' is best at the frequency range 0.02–0.32 ω_{ce}; (3) the PSD increases with J', following the power function $\text{PSD} = J'^k \cdot e^b$ ($k > 0$); and (4) the PSD of lower-frequency fluctuation varies more dramatically with J'. The strong J' tends to occur at the intense current filament (Figures 1(g) and (i)), owing to the sharp current-density gradient at the current filament. Therefore, the strong J' also primarily occurs at the "O-line" topology. These results can significantly advance our understanding of magnetic reconnection and turbulence.

The slope (S_{PSD}) of the PSD, namely spectral power law, can reflect the scale of energy dissipation. Stawarz et al. (2019) presented statistics of current structures in magnetosheath turbulence, and found a steeper spectral power law in the interval with more intense current density (see Figures 2 and 3 in Stawarz et al. 2019 for details). The existence of intense current density can lead to large current-density variations (J'), owing to the sharp current-density gradient at these intense current structures. As a consequence, there may be also relations between the spectral power law and J'. In our study, the S_{PSD} decreases linearly with the logarithm of J', suggesting that large J' steepens the spectral index and has effects on the dissipation scale. The steepening of spectral index may be caused by reconnection in these current structures or a change in the nonlinear dynamics (Stawarz et al. 2019). In our study, the large J' primarily occurs at spiral nulls (Figure 2), indicating that reconnection may not be responsible for the steepening.

Simulations have demonstrated that the kinetic-scale turbulence is driven by electron shear instability (Che et al. 2011; Jain et al. 2017), which is excited by the flow-velocity gradients. In the IDR, the current is primarily carried by electrons, suggesting that the electron flow-velocity gradients are approximately equated with the current-density gradients. In addition, the current-density gradients can lead to strongly turbulent states of current layers (Coppi 1965; Drake et al. 1994). Therefore, the current-density gradients may correlate with the turbulence. In this event, we cannot obtain the current-density gradients, due to a lack of high-resolution plasma measurements. Therefore, we substitute the current-density variations (J') for the current-density gradients, and find that the current-density variations indeed correlate with the turbulence.

Since the plasma flow speed is much larger than the spacecraft speed, we assume that the spacecraft is static in the IDR. Therefore, $\frac{dJ}{dt}$ represents the total derivative of current density, containing temporal variations and spatial variations. In high-speed flows, the Taylor hypothesis (Pucci et al. 2018) assumes that current-density variations at an observational point are predominantly due to the rapid sweeping of spatial structures, i.e., $\frac{dJ}{dt} = \boldsymbol{V} \cdot \nabla J$, where $\boldsymbol{V}$ is flow velocity and ∇J is current-density gradient. Therefore, the current-density variation only contains spatial variation. However, the Taylor hypothesis may be invalid in this event, because the kinetic-

scale turbulence develops fast. Therefore, we cannot distinguish the spatial variation from the temporal variation of current density. In order to address the problem, spacecraft missions with high-resolution plasma measurements, e.g., *MMS* (Burch et al. 2016a), are necessary. In future work, we will use *MMS* data to study such relationships between current filaments and turbulence.

We thank the *Cluster* team for providing the data for this study. *Cluster* data are available at https://csa.esac.esa.int/csa/aio/. This work was supported by NSFC grants 41404133, 41874188, 41574153, 40621003, and 41431071, and the ISSI travel grant for team "Magnetic Topology Effects on Energy Dissipation in Turbulent Plasma."

ORCID iDs

Z. Z. Chen https://orcid.org/0000-0003-0980-5350
T. Y. Wang https://orcid.org/0000-0003-3072-6139

References

Alexandrova, O., Chen, C. H. K., Sorriso-Valvo, L., Horbury, T. S., & Bale, S. D. 2013, SSRv, 178, 101
Angelopoulos, V., McFadden, J. P., Larson, D., et al. 2008, Sci, 321, 931
Borovsky, J. E., Elphic, R. C., Funsten, H. O., & Thomsen, M. F. 1997, JPIPh, 57, 1
Burch, J. L., Moore, T. E., Torbert, R. B., & Giles, B. L. 2016a, SSRv, 199, 5
Burch, J. L., Torbert, R. B., Phan, T. D., et al. 2016b, Sci, 352, aaf2939
Cao, D., Fu, H. S., Cao, J. B., et al. 2017, GeoRL, 44, 3954
Che, H., Drake, J. F., & Swisdak, M. 2011, Natur, 474, 184
Chen, C. H. K. 2016, JPIPh, 82, 535820602
Chen, G., Fu, H. S., Zhang, Y., et al. 2019a, ApJL, 881, L8
Chen, L.-J., Hesse, M., Wang, S., Bessho, N., & Daughton, W. 2016, GeoRL, 43, 2405
Chen, P. F., & Shibata, K. 2000, ApJ, 545, 524
Chen, X. H., Fu, H. S., Liu, C. M., et al. 2018, ApJ, 852, 17
Chen, Z. Z., Fu, H. S., Liu, C. M., et al. 2019b, GeoRL, 46, 5698
Chen, Z. Z., Fu, H. S., Wang, Z., Liu, C. M., & Xu, Y. 2019c, GeoRL, 46, 10209
Chen, Z. Z., Fu, H. S., Wang, T. Y., et al. 2019d, Science China Technological Sciences, 62, 144
Coppi, B. 1965, PhFl, 8, 2273
Daughton, W., Nakamura, T. K. M., Karimabadi, H., et al. 2014, PhPl, 21, 052307
Daughton, W., Roytershteyn, V., Karimabadi, H., et al. 2011, NatPh, 7, 539
Drake, J. F., Gerber, J., & Kleva, R. G. 1994, JGR, 99, 11211
Dunlop, M. W., Balogh, A., & Glassmeier, K.-H. 2002, JGRA, 107, 1385
Eastwood, J. P., Phan, T. D., Bale, S. D., & Tjulin, A. 2009, PhRvL, 102, 035001
Eastwood, J. P., Phan, T. D., Øieroset, M., & Shay, M. A. 2010, JGRA, 115, A08215
Ergun, R. E., Goodrich, K. A., Wilder, F. D., et al. 2018, GeoRL, 45, 3338
Escoubet, C. P., Fehringer, M., & Goldstein, M. 2001, AnGeo, 19, 1197
Fu, H. S., Cao, J. B., Cao, D., et al. 2019a, GeoRL, 46, 48
Fu, H. S., Cao, J. B., Khotyaintsev, Y. V., et al. 2013a, GeoRL, 40, 6023
Fu, H. S., Cao, J. B., Vaivads, A., et al. 2016, JGRA, 121, 1263
Fu, H. S., Khotyaintsev, Y. V., André, M., & Vaivads, A. 2011, GeoRL, 38, L16104
Fu, H. S., Khotyaintsev, Y. V., Vaivads, A., et al. 2012a, JGRA, 117, A12221
Fu, H. S., Khotyaintsev, Y. V., Vaivads, A., et al. 2012b, GeoRL, 39, L10101
Fu, H. S., Khotyaintsev, Y. V., Vaivads, A., et al. 2013b, NatPh, 9, 426
Fu, H. S., Peng, F. Z., Liu, C. M., et al. 2019b, GeoRL, 46, 5645
Fu, H. S., Vaivads, A., Khotyaintsev, Y. V., et al. 2015, JGRA, 120, 3758
Fu, H. S., Vaivads, A., Khotyaintsev, Y. V., et al. 2017, GeoRL, 44, 37
Fu, H. S., Xu, Y., Vaivads, A., & Khotyaintsev, Y. V. 2019c, ApJL, 870, L22
Fuselier, S. A., Vines, S. K., Burch, J. L., et al. 2017, JGRA, 122, 5466
Gosling, J. T., Skoug, R. M., McComas, D. J., & Smith, C. W. 2005, JGRA, 110, A01107
Guo, F., & Giacalone, J. 2015, ApJ, 802, 97
Guo, F., Liu, Y.-H., Daughton, W., & Li, H. 2015, ApJ, 806, 167
He, J. S., Duan, D., Wang, T. Y., et al. 2019, ApJ, 880, 121
He, J. S., Marsch, E., Tu, C. Y., & Tian, H. 2009, ApJL, 705, L217
Huang, S. Y., Jiang, K., Yuan, Z. G., et al. 2019, GeoRL, 46, 580
Huang, S. Y., Sahraoui, F., Deng, X. H., et al. 2014, ApJL, 789, L28
Jain, N., Von Stechow, A., MuñOz, P. A., et al. 2017, PhPl, 24, 092312
Karimabadi, H., Roytershteyn, V., Daughton, W., & Liu, Y.-H. 2013, SSRv, 178, 307
Lazarian, A., & Vishniac, E. T. 1999, ApJ, 517, 700
Li, X., Dasgupta, B., & Li, G. 2014, AdSpR, 53, 1153
Li, X., Guo, F., Li, H., & Li, G. 2015, ApJL, 811, L24
Liu, C. M., Chen, Z. Z., Wang, Z., & Liu, Y. Y. 2019a, ApJ, 871, 209
Liu, C. M., Vaivads, A., Graham, D. B., et al. 2019b, GeoRL, 46, 12702
Liu, C. M., & Fu, H. S. 2019, ApJL, 873, L2
Liu, C. M., Fu, H. S., Cao, D., Xu, Y., & Divin, A. 2018a, ApJ, 860, 128
Liu, C. M., Fu, H. S., Xu, Y., et al. 2018b, GeoRL, 45, 4628
Liu, Y.-H., Daughton, W., Karimabadi, H., et al. 2013, PhRvL, 110, 265004
Liu, Y. Y., Fu, H. S., Liu, C. M., et al. 2019c, ApJL, 877, L16
Liu, Y. Y., Fu, H. S., Olshevsky, V., et al. 2019d, ApJS, 244, 31
Lu, S., Angelopoulos, V., Artemyev, A. V., et al. 2019, ApJ, 878, 109
Øieroset, M., Phan, T. D., Fujimoto, M., et al. 2001, Natur, 412, 414
Olshevsky, V., Divin, A., Eriksson, E., Markidis, S., & Lapenta, G. 2015, ApJ, 807, 155
Olshevsky, V., Lapenta, G., & Markidis, S. 2013, PhRvL, 111, 045002
Olshevsky, V., Servidio, S., Pucci, F., Primavera, L., & Lapenta, G. 2018, ApJ, 860, 11
Parnell, C. E., Smith, J. M., Neukirch, T., & Priest, E. R. 1996, PhPl, 3, 759
Peng, F. Z., Fu, H. S., Cao, J. B., et al. 2017, JGRA, 122, 6349
Pontin, D. I. 2011, AdSpR, 47, 1508
Pontin, D. I., & Craig, I. J. D. 2006, ApJ, 642, 568
Pucci, F., Matthaeus, W. H., Chasapis, A., et al. 2018, ApJ, 867, 10
Retinò, A., Sundkvist, D., Vaivads, A., et al. 2007, NaPh, 3, 236
Sahraoui, F., Goldstein, M. L., Robert, P., et al. 2009, PhRvL, 102, 231102
Stawarz, J. E., Eastwood, J. P., Phan, T. D., et al. 2019, ApJL, 877, L37
Torbert, R. B., Burch, J. L., Phan, T. D., et al. 2018, Sci, 362, 1391
Tu, C.-Y., & Marsch, E. 1995, SSRv, 73, 1
Vörös, Z., Yordanova, E., Varsani, A., et al. 2017, JGRA, 122, 11442
Wan, M., Matthaeus, W. H., Roytershteyn, V., et al. 2015, PhRvL, 114, 175002
Wang, J., Cao, J. B., Fu, H. S., Liu, W. L., & Lu, S. 2017, JGRA, 122, 185
Wang, T., Cao, J., Fu, H., Meng, X., & Dunlop, M. 2016, GeoRL, 43, 1854
Wang, Z., Fu, H. S., Liu, C. M., et al. 2019, GeoRL, 46, 1195
Webster, J. M., Burch, J. L., Reiff, P. H., et al. 2018, JGRA, 123, 4858
Xu, Y., Fu, H. S., Liu, C. M., & Wang, T. Y. 2018a, ApJ, 853, 11
Xu, Y., Fu, H. S., Norgren, C., Hwang, K.-J., & Liu, C. M. 2018b, PhPl, 25, 072123
Yamada, L., Kulsrud, R., & Ji, H. 2010, RvMP, 82, 603
Yang, J., Cao, J. B., Fu, H. S., et al. 2017, JGRA, 122, 4299
Zhu, B., Yan, H., Zhong, Y., et al. 2020, Applied Mathematical Modelling, 78, 968
Zhu, B. J., Yan, H., Yuen, D. A., & Shi, Y. L. 2019, E&PP, 3, 17